Compressive Sensing Techniques for Enhanced Near Field Antenna Evaluation

M. Salucci, N. Anselmi, and A. Massa

2024/04/05

Contents

1 Test Case 4: *AUT* with only a magnitude failure affecting the 3^{rd} row ($\nu^{(3)} = 0.45$); incremented failure ranges to build the over-complete basis ($\nu^{(s)} \in [0.0,\, 1.0]\,,\ F^{(s)} = 7$ and $\gamma^{(s)} \in [-\pi,\, \pi]\,,\ P^{(s)} = 5$)

Parameters

Gold Antenna (Without Defects)

- Geometry : Planar array of microstrip patches on the (x, y) plane;
- Working Frequency : $f = 3.6\,[GHz]$ ($\lambda = 83.27 \times 10^{-3}\,[m]$ in free space);
- Substrate (PEC-backed) :
  - Dimensions : infinite;
  - Relative Permittivity : $\varepsilon_{r,sub} = 4.7$;
  - Loss Tangent : $tan\,\delta_{sub} = 0.014$;
  - Thickness : $h_{sub} = 0.019\,[\lambda]$ $(1.6\,[mm])$;
- Microstrip patches :
  - Dimensions : $l_x \approx 0.22\,[\lambda]$ $(18.16\ [mm])$, $l_y \approx 0.33\,[\lambda]$ $(27.25\ [mm])$;
  - Feeding : pin-fed;
- Spacing between elements : $d_x = d_y = \frac{\lambda}{2}$;
- Number of elements in each row : $N_x = 6$;
- Number of elements in each column : $N_y = 10$;
- Total number of elements : $N = (N_x \times N_y) = 60$;
- Total size of the antenna : $L_x = 5\,[\lambda]$, $L_y = 9\,[\lambda]$;
- Element excitations : $w_n^{(s)} = 1.0 + j0.0,\ n = 1, ..., N^{(s)},\ s = 1, ..., S$;

Antenna Under Test (AUT - With Defects)

1. Failures of the excitation magnitude of the 3^{rd} row;
   - Failure factor of the elements in the 3^{rd} row $(s = 3)$: $\nu^{(3)} = 0.45$;

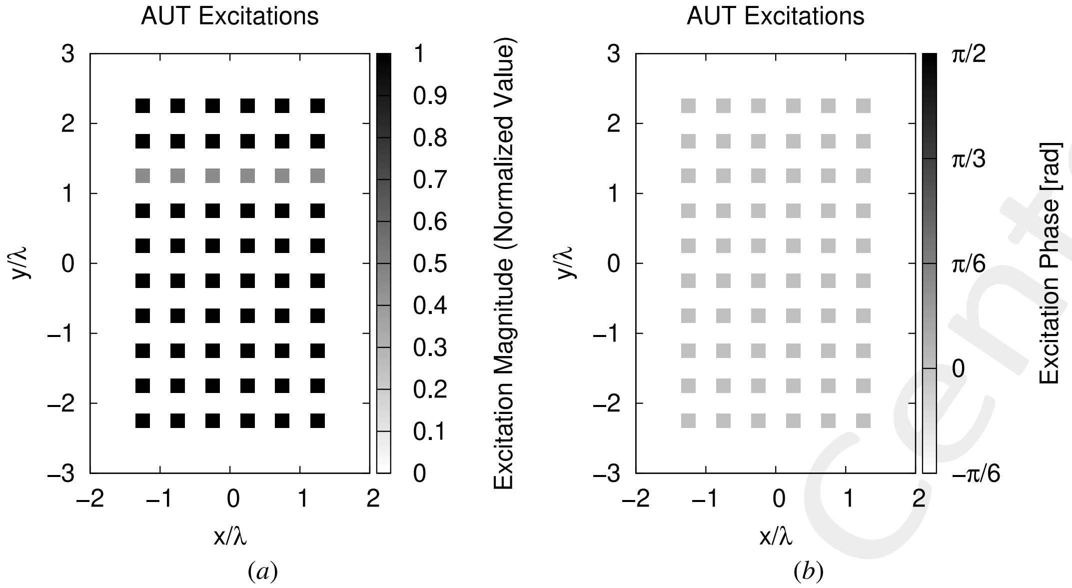

Figure 1: (a) Magnitude of the element excitations in the *AUT* ($\nu^{(3)} = 0.45$), (b) phase of the element excitations in the *AUT* .

Measurement Set-Up

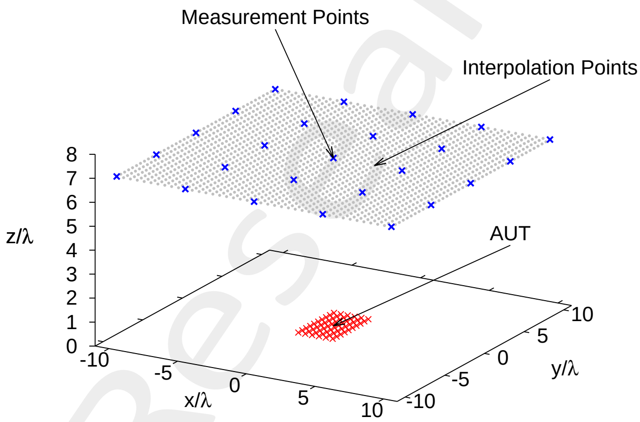

Figure 2: Disposition of the interpolation points ($T = 1681$) and of the measurement points ($M = 25$) in the near-field region of the *AUT*

- Type of measurements : near-field;
- Height of the measurement region : $H = 7\,[\lambda]$;
- Interpolation points :
  - Number of points : $T = 41 \times 41 = 1681$;
  - Coordinates : $x_t \in [-10,\, 10]\,[\lambda],\;\; y_t \in [-10,\, 10]\,[\lambda],\;\; z_t = H\,[\lambda],\;\; t = 1, ..., T$;
  - Interpolation step : $\Delta^{int}_{x/y} = 0.5\,[\lambda]$;
- Measurement points :
  - Coordinates : $x^{meas}_m \in [-10,\, 10]\,[\lambda],\;\; y^{meas}_m \in [-10,\, 10]\,[\lambda],\;\; z^{meas}_m = H\,[\lambda],\;\; m = 1, ..., M$;

- Number of points : $M_{x/y} = 5 \rightarrow M = 25$;
- Measurement step : $\Delta_{x/y}^{meas} = 5\,[\lambda]$
- Ratio between number of measurements and total number of elements : $(M/N) = 0.42$;

Measurement-by-Design Technique

- Number of generated bases : $B = 20$;
- Bases $b = 1, ..., 10$: magnitude failures in each row ($s = 1, ..., 10$)
  - **Failure factor of the elements :** $\nu^{(s)} \in [0.0,\, 1.0],\;\; s = 1, ..., 10$;
  - Number of simulated failure factors : $F^{(s)} = 7,\; s = 1, ..., 10$;
- Bases $b = 11, ..., 20$: phase failures in each row ($s = 1, ..., 10$)
  - **Phase shift of the elements :** $\gamma^{(s)} \in [-\pi,\, \pi]\,[rad],\;\; s = 1, ..., 10$;
  - Number of simulated phase shifts: $P^{(s)} = 5,\;\; s = 1, .., 10$;
- Threshold on the singular values magnitude (normalized) : $\eta = -40\,[dB]$;
- Total number of simulated AUT configurations : $K = S \times (F^{(s)} + P^{(s)}) = 10 \times (7 + 5) = 120$;

Dimension of the Over-Complete Basis

The dimension of the over-complete basis is

$$Q = 40$$

This number is given by the sum of the vectors belonging to the two considered bases:

1. Magnitude failures : $Q_1, ..., Q_{10} = 2$;
2. Phase failures : $Q_{11}, ..., Q_{20} = 2$.

Alternative (*BCS*) MbD parameters

- Toleration factor for *BCS* solver: $Tolerance = 1 \times 10^{-8}$;
- Initial noise variance for *BCS* solver: $\eta_0^{opt_1} = 10^{-2}$ and $\eta_0^{opt_2} = 5 \times 10^{-4}$. This values have been obtained as a result of a calibration procedure;

Original (*OMP*) MbD parameters

- Max. number of iterations of the OMP algorithm : $I = \{1;\, 2;\, 3;\, ...;\, 10\}$;
- Selected iteration to report the results: $I = 6$; this choice is justified by the fact that at this iteration the *OMP* algorithm reaches the best near field error as shown in the following Fig. 3.

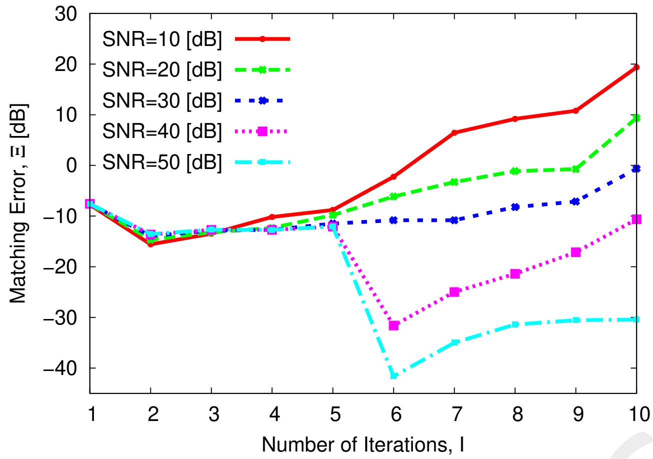

Figure 3: Behaviour of the near-field matching error versus the number of *OMP* iterations, I.

Noise

- SNR on the measured data : $SNR = \{50;\ 40;\ 30;\ 20;\ 10\}\ [dB]$;
- Noise seed : $Noise\_Seed = 11$.

1.1 Comparison between original (*OMP*) and alternative (*BCS*) MbD

Near-Field Error

The comparison, in terms of near field error, between the original (*OMP*) and the alternative (*BCS*) MbD is reported in the following Fig. 4.

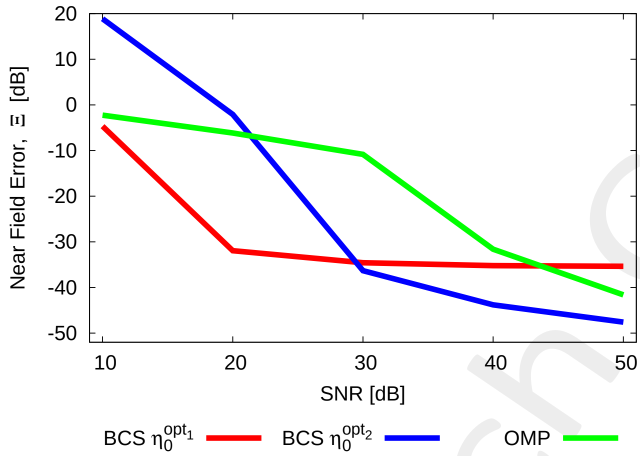

Figure 4: Near Field Error comparison between original (*OMP*) and alternative (*BCS*) MbD for different SNR values.

$SNR\,[dB]$	*Near Field Error,* $\Xi\ [dB]$		
	BCS		OMP
	$\eta_0^{opt_1}$	$\eta_0^{opt_2}$	
50	-35.36	-47.59	-41.61
40	-35.21	-43.80	-31.61
30	-34.58	-36.32	-10.82
20	-31.93	-2.09	-6.15
10	-4.67	18.89	-2.24

Table I: Near Field Errors obtained by the original (*OMP*) and alternative (*BCS*) MbD

Observations

- The *OMP* algorithm performs poorly for $SNR \leq 30\,[dB]$ where obtains an error $\Xi \geq -10\,[dB]$ leading to an error difference up to $\simeq 25\,[dB]$ compared to the *BCS* results at $SNR = 30\,[dB]$. However, for $SNR \geq 40\,[dB]$ the *OMP* results are comparable to those of the *BCS*;
- About the *BCS* solver:
  - using $\eta_0^{opt_1}$, the *BCS* algorithm achieves the best results for $SNR \leq 30\,[dB]$, in particular at $SNR = 20\,[dB]$ where its error is more than $25\,[dB]$ lower than that of the others. After that the behaviour of the error of this *BCS* version is quite flat which leads to obtain the higher error for $SNR = 50\,[dB]$;
  - using $\eta_0^{opt_2}$, the *BCS* solver obtains the worst result if compared to both the other methods for $SNR \leq 20\,[dB]$ but for higher SNR values it performs good and achieves the best results for $SNR \geq 30\,[dB]$.

Estimated Near-Field

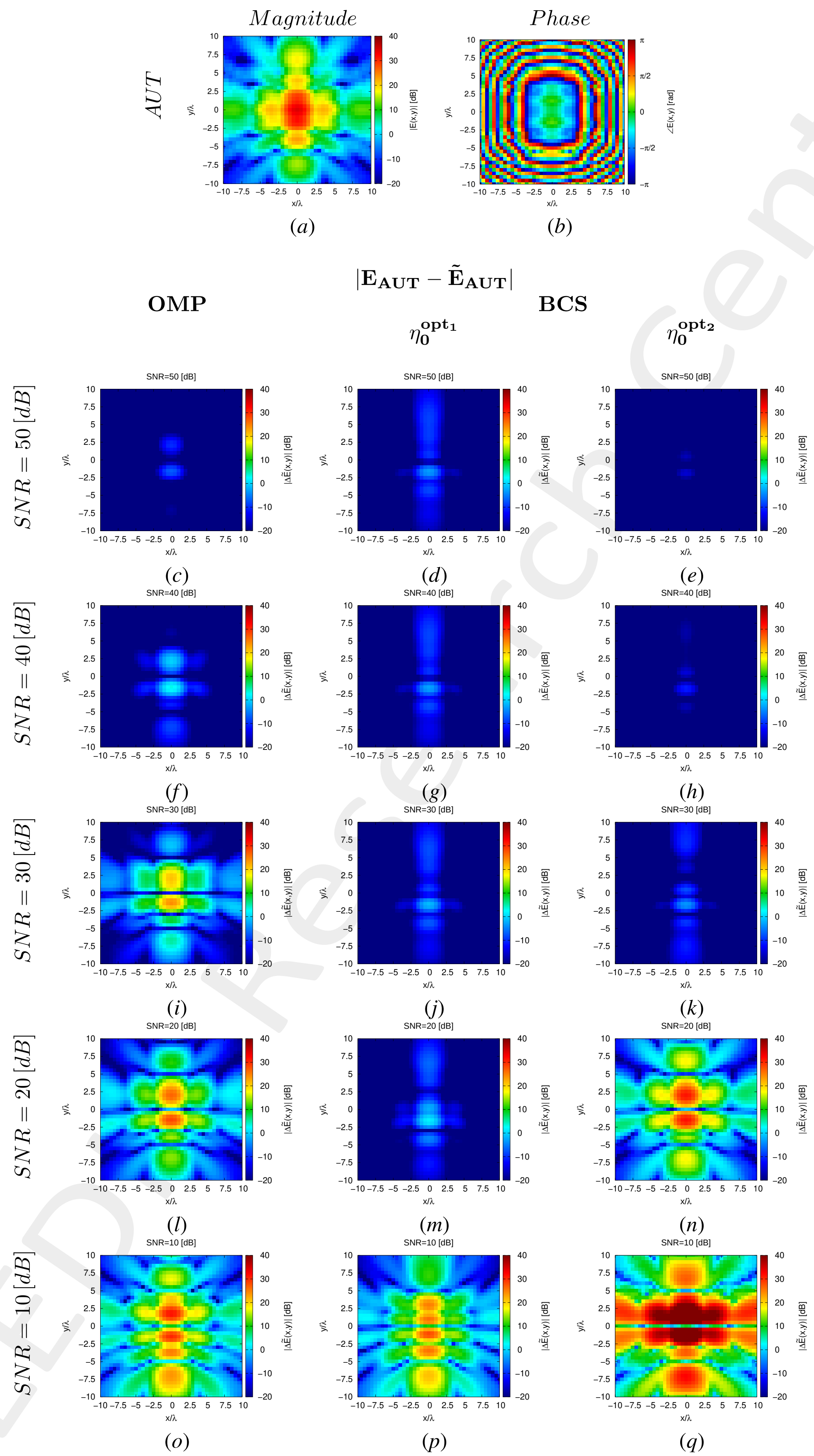

Figure 5: Magnitude difference between the actual and estimated $2-D$ near-field pattern when processing noisy measurements at different SNRs.

Estimated Coefficients

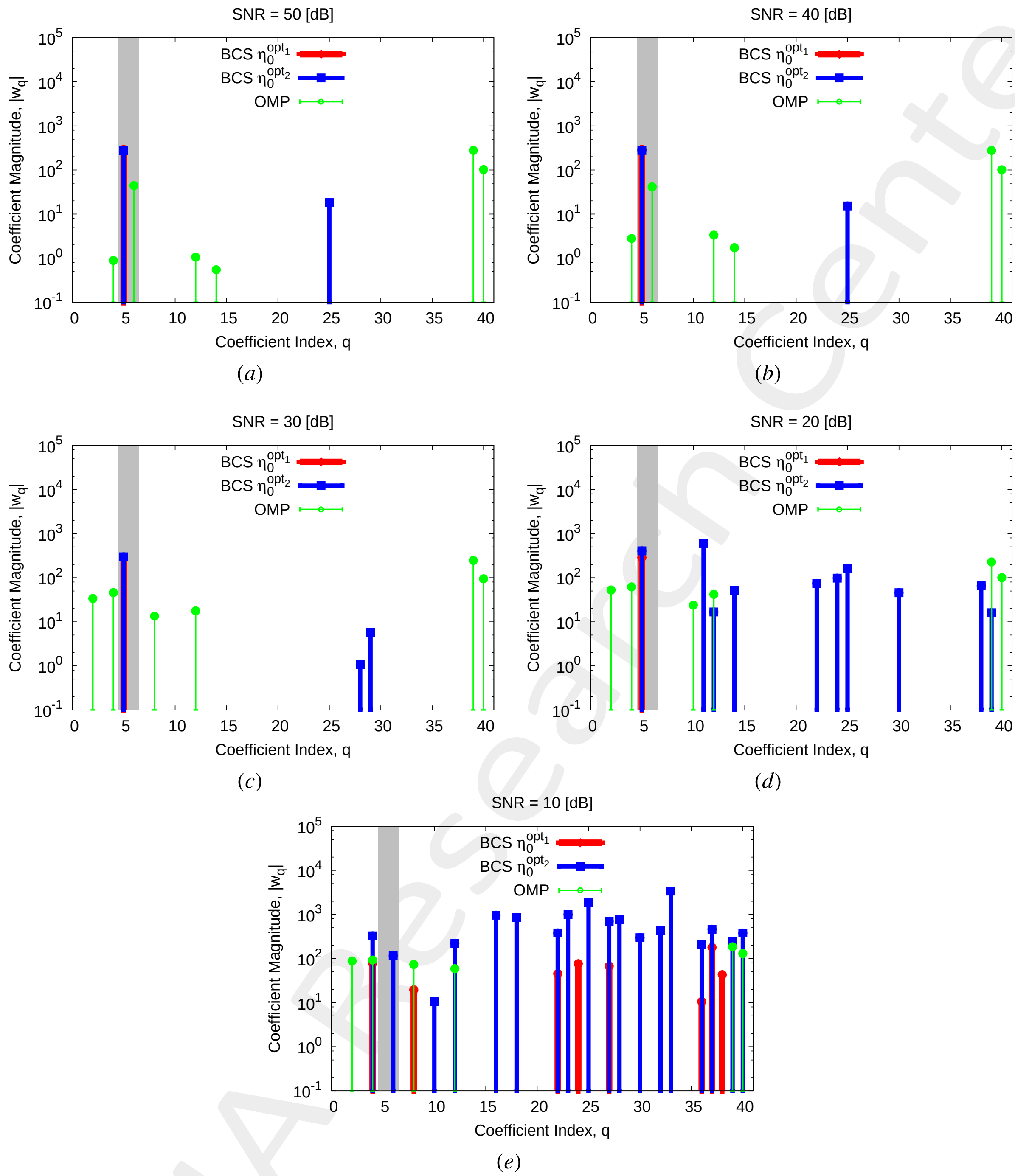

Figure 6: Coefficient comparison between original (*OMP*) and alternative (*BCS*) MbD : (*a*) $SNR = 50\,[dB]$, (*b*) $SNR = 40\,[dB]$, (*c*) $SNR = 30\,[dB]$, (*d*) $SNR = 20\,[dB]$, (*e*) $SNR = 10\,[dB]$

- The *AUT* is affected only by a magnitude failure of the 3^{rd} row and the *OMP* solver is able to correctly detect this failure for $SNR \geq 40\,[dB]$, even if other vectors are also selected. Moreover, 3 out of the 6 selected vectors are always the same independently from the SNR value (vector indexes $q = 12,\ 39,\ 40$);
- The *BCS* algorithm, when $\eta_0^{opt_2}$ is used, presents a solution which is not sparse for $SNR \leq 20\,[dB]$ but becomes sparse as the *SNR* value increases; moreover, this *BCS* version correctly detects the magnitude failure affecting the *AUT* with an accuracy that increases as the *SNR* increases. Instead, when $\eta_0^{opt_2}$ is used, the *BCS* failure detection is

extremely precise already for $SNR \geq 20\,[dB]$.

1.1.1 OMP vs best BCS

The main idea of this section is to compare the performance of the *OMP* algorithm and the best *BCS* configuration.

Near-Field Error

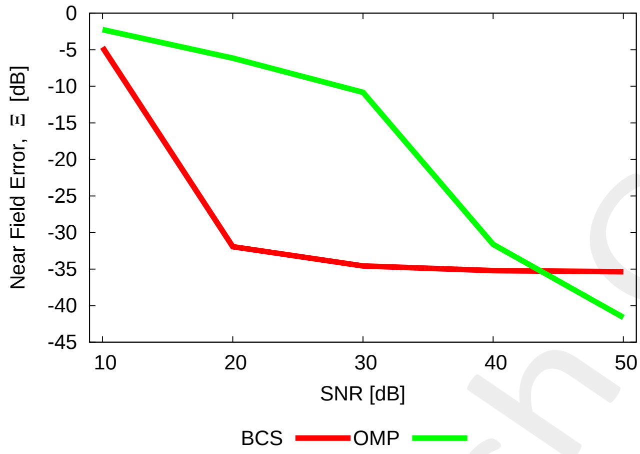

Figure 7: Near Field Error comparison between original (*OMP*) and alternative (*BCS*) MbD for different SNR values.

$SNR\,[dB]$	*Near Field Error*, Ξ $[dB]$	
	BCS	OMP
50	-35.36	-41.61
40	-35.21	-31.61
30	-34.58	-10.82
20	-31.93	-6.15
10	-4.67	-2.24

Table II: Near Field Errors obtained by the original (*OMP*) and alternative (*BCS*) MbD

Estimated Far-Field

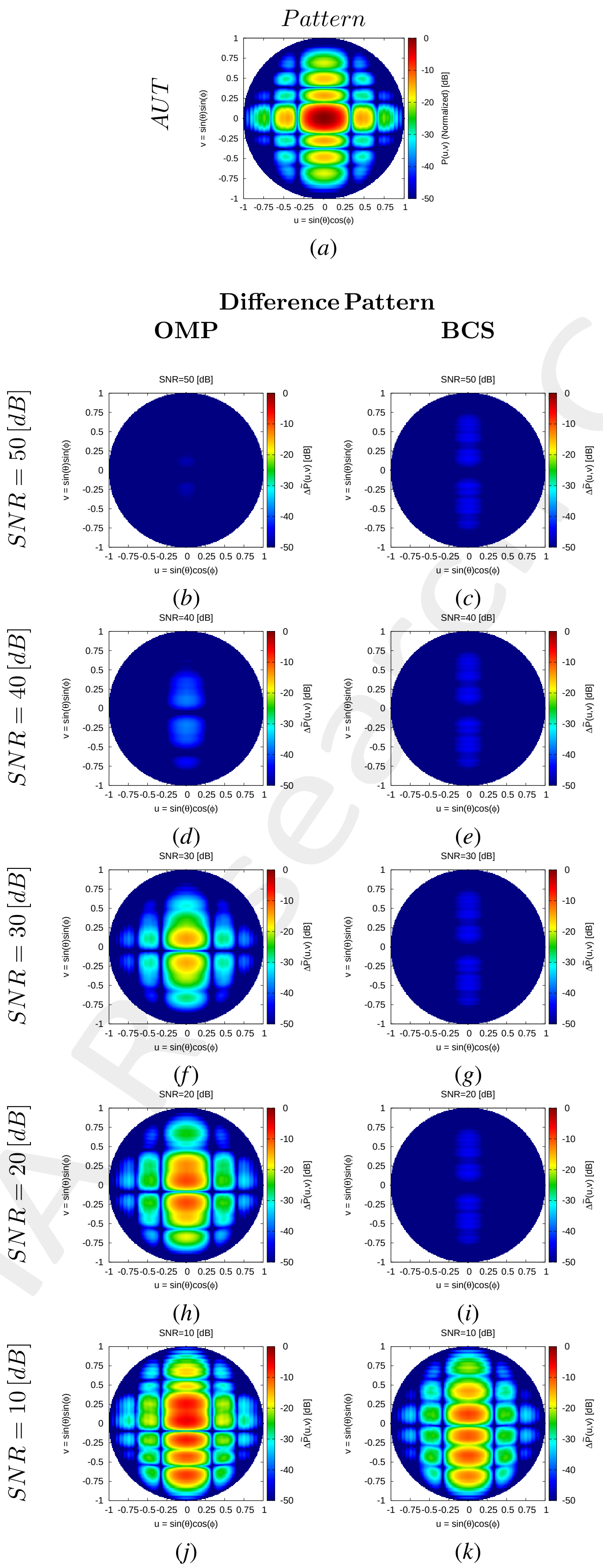

Figure 8: Difference between the actual and estimated $2-D$ far-field pattern when processing noisy measurements at different SNRs.

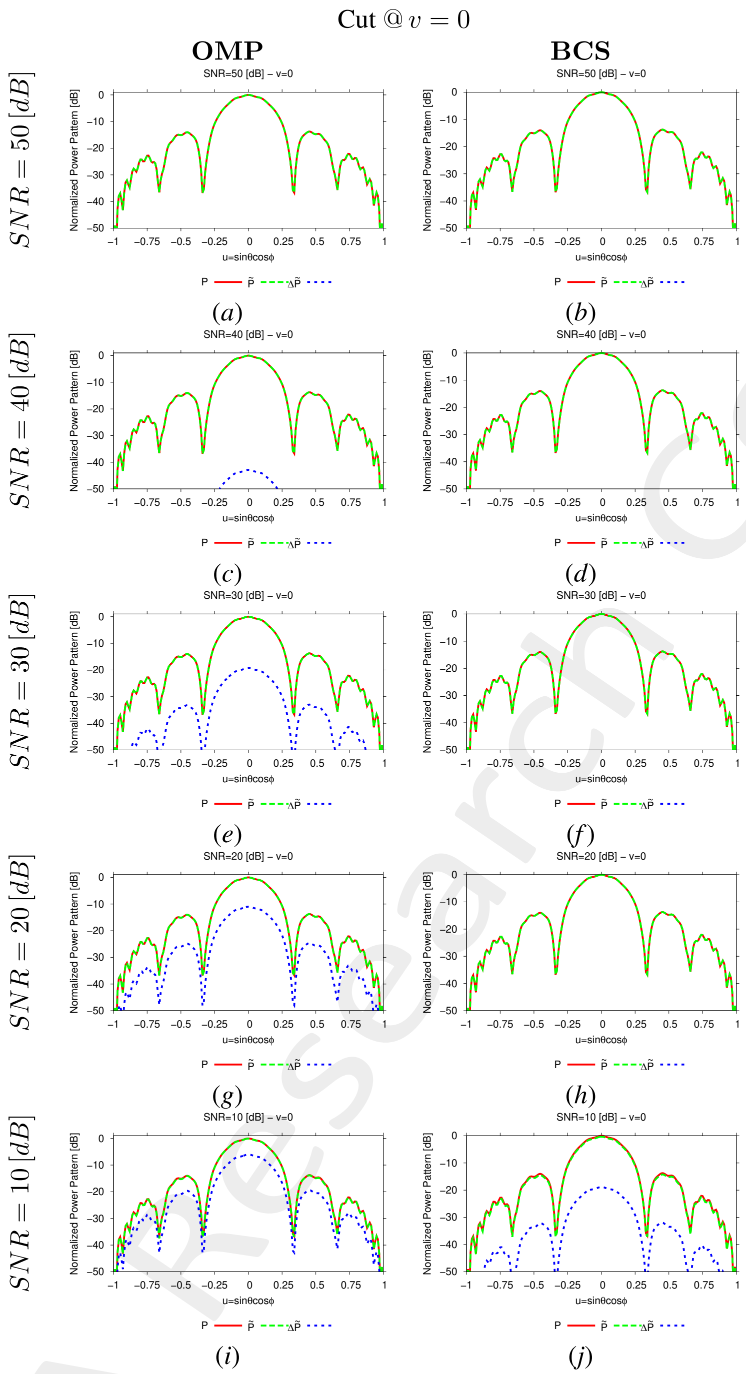

Figure 9: $1-D$ cuts of the estimated far-field pattern (obtained through near-to-far-field transformation from the estimated near-field patterns) under several noisy conditions

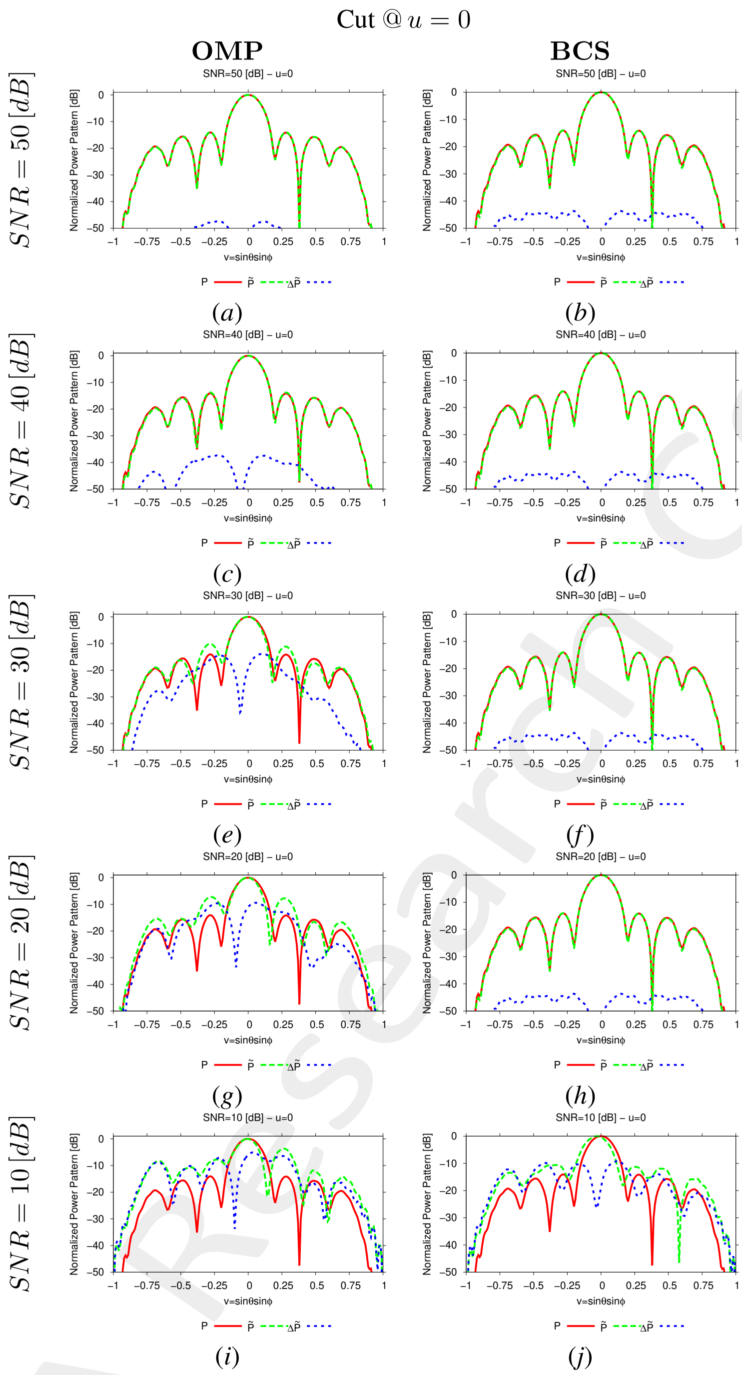

Figure 10: $1-D$ cuts of the estimated far-field pattern (obtained through near-to-far-field transformation from the estimated near-field patterns) under several noisy conditions

$SNR\,[dB]$	$Far - Field\,Error,\ \chi\ [dB]$	
	BCS	OMP
50	-36.69	-42.55
40	-36.69	-32.52
30	-36.69	-10.82
20	-36.69	-5.82
10	-4.90	-1.41

Table III: Far-field matching error between the actual and estimated AUT patterns (both obtained through near-to-far-field transformation from the corresponding near-field patterns) under several noisy conditions.

Estimated Coefficients

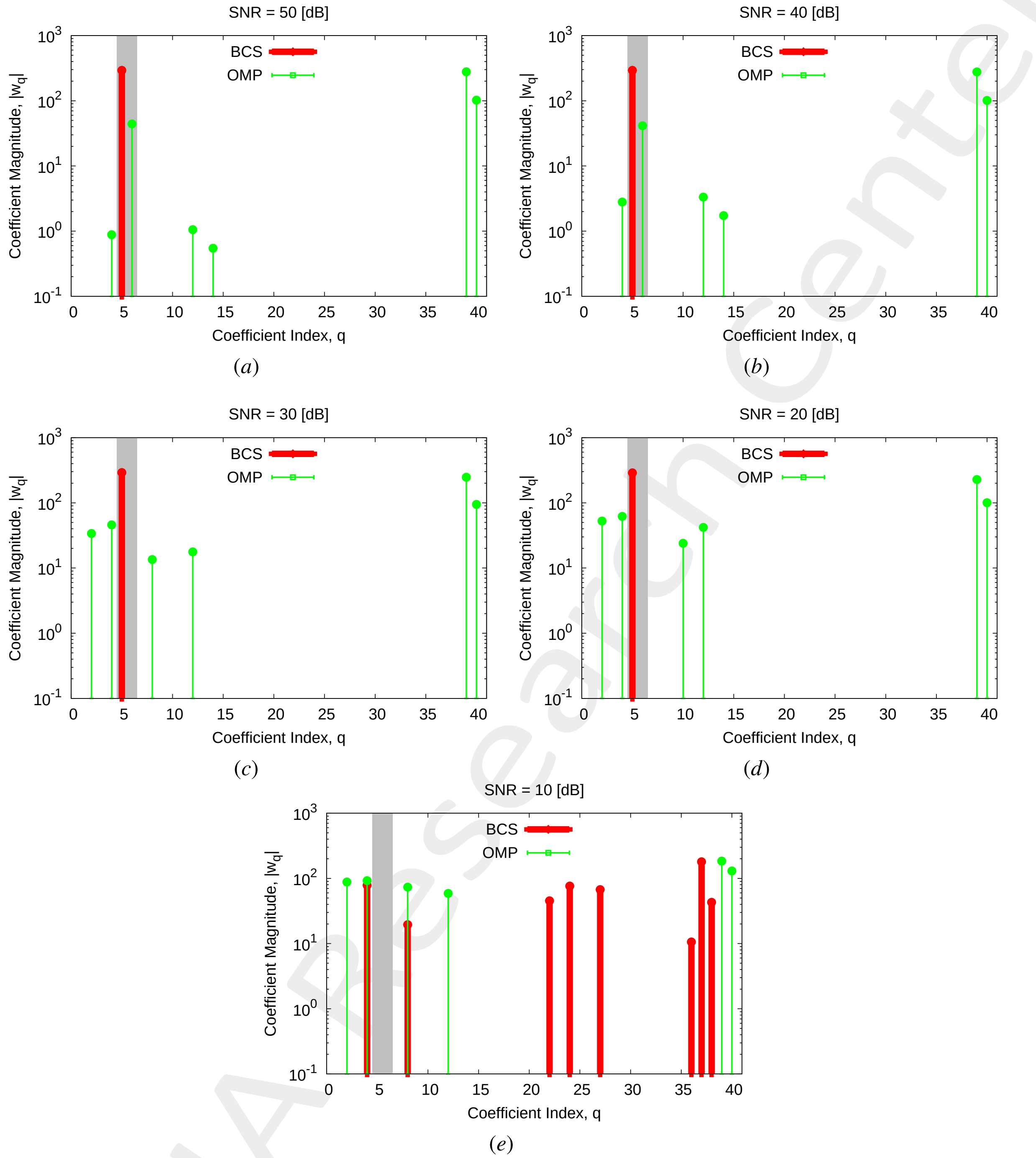

Figure 11: Coefficient comparison between original (*OMP*) and alternative (*BCS*) MbD: (*a*) $SNR = 50\,[dB]$, (*b*) $SNR = 40\,[dB]$, (*c*) $SNR = 30\,[dB]$, (*d*) $SNR = 20\,[dB]$, (*e*) $SNR = 10\,[dB]$

2 Test Case 5: *AUT* with only a phase shift affecting the 3^{rd} row ($\gamma^{(3)} = \frac{\pi}{3}$); incremented failure ranges to build the over-complete basis ($\nu^{(s)} \in [0.0,\, 1.0]\,,\ F^{(s)} = 7$ and $\gamma^{(s)} \in [-\pi,\, \pi]\,,\ P^{(s)} = 5$)

Parameters

Gold Antenna (Without Defects)

- Geometry : Planar array of microstrip patches on the (x, y) plane;
- Working Frequency : $f = 3.6\,[GHz]$ ($\lambda = 83.27 \times 10^{-3}\,[m]$ in free space);
- Substrate (PEC-backed) :
  - Dimensions : infinite;
  - Relative Permittivity : $\varepsilon_{r,sub} = 4.7$;
  - Loss Tangent : $tan\,\delta_{sub} = 0.014$;
  - Thickness : $h_{sub} = 0.019\,[\lambda]\ (1.6\,[mm])$;
- Microstrip patches :
  - Dimensions : $l_x \approx 0.22\,[\lambda]\ (18.16\ [mm]),\ l_y \approx 0.33\,[\lambda]\ (27.25\ [mm])$;
  - Feeding : pin-fed;
- Spacing between elements : $d_x = d_y = \frac{\lambda}{2}$;
- Number of elements in each row : $N_x = 6$;
- Number of elements in each column : $N_y = 10$;
- Total number of elements : $N = (N_x \times N_y) = 60$;
- Total size of the antenna : $L_x = 5\,[\lambda],\ L_y = 9\,[\lambda]$;
- Element excitations : $w_n^{(s)} = 1.0 + j0.0,\ n = 1, ..., N^{(s)},\ s = 1, ..., S$;

Antenna Under Test (AUT - With Defects)

1. Failures of the excitation phase of the 3^{rd} row;
   - Phase shift of the elements in the 3^{rd} row ($s = 3$) : $\gamma^{(3)} = \frac{\pi}{3}\,[rad]$;

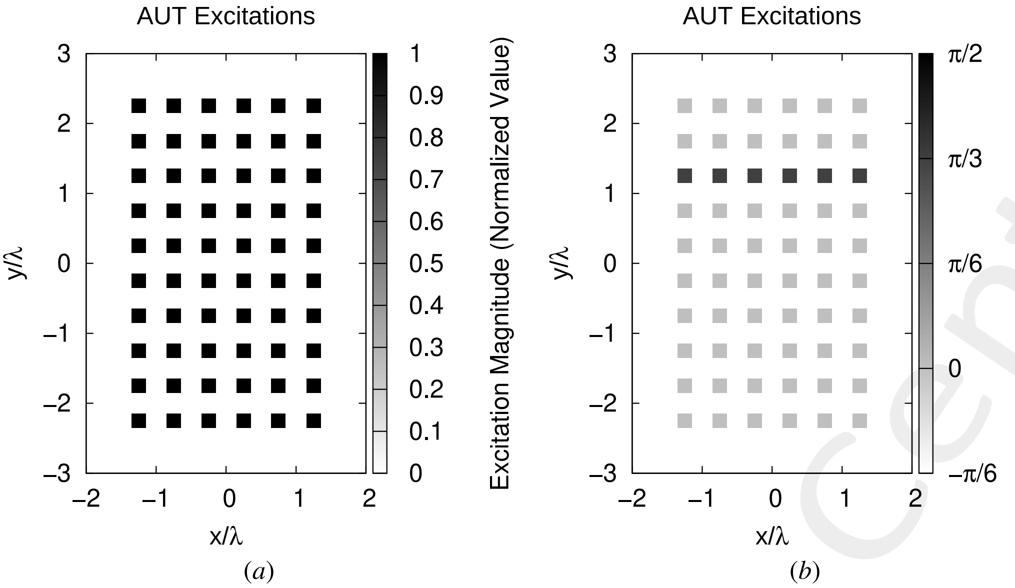

Figure 12: (a) Magnitude of the element excitations in the AUT , (b) phase of the element excitations in the AUT ($\gamma^{(3)} = \frac{\pi}{3}\,[rad]$).

Measurement Set-Up

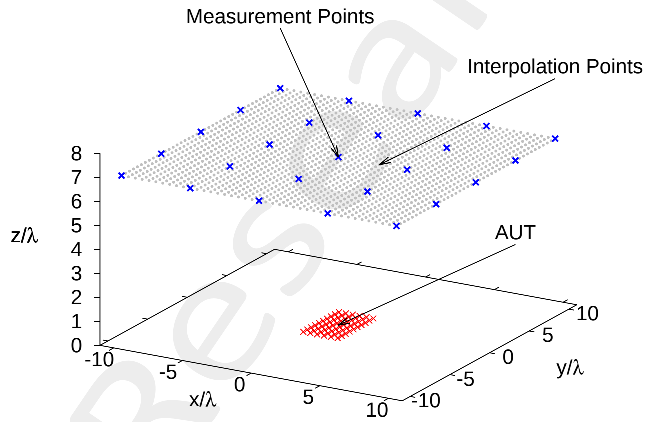

Figure 13: Disposition of the interpolation points ($T = 1681$) and of the measurement points ($M = 25$) in the near-field region of the AUT

- Type of measurements : near-field;
- Height of the measurement region : $H = 7\,[\lambda]$;
- Interpolation points :
  - Number of points : $T = 41 \times 41 = 1681$;
  - Coordinates : $x_t \in [-10,\,10]\,[\lambda],\;\; y_t \in [-10,\,10]\,[\lambda],\;\; z_t = H\,[\lambda],\;\; t = 1, ..., T$;
  - Interpolation step : $\Delta^{int}_{x/y} = 0.5\,[\lambda]$;
- Measurement points :
  - Coordinates : $x^{meas}_m \in [-10,\,10]\,[\lambda],\;\; y^{meas}_m \in [-10,\,10]\,[\lambda],\;\; z^{meas}_m = H\,[\lambda],\;\; m = 1, ..., M$;

  - Number of points : $M_{x/y} = 5 \rightarrow M = 25$;
  - Measurement step : $\Delta_{x/y}^{meas} = 5\,[\lambda]$
  - Ratio between number of measurements and total number of elements : $(M/N) = 0.42$;

Measurement-by-Design Technique

- Number of generated bases : $B = 20$;
- Bases $b = 1, ..., 10$: magnitude failures in each row ($s = 1, ..., 10$)
  - **Failure factor of the elements :** $\nu^{(s)} \in [0.0,\ 1.0],\ \ s = 1, ..., 10$;
  - Number of simulated failure factors : $F^{(s)} = 7,\ s = 1, ..., 10$;
- Bases $b = 11, ..., 20$: phase failures in each row ($s = 1, ..., 10$)
  - **Phase shift of the elements :** $\gamma^{(s)} \in [-\pi,\ \pi]\,[rad],\ \ s = 1, ..., 10$;
  - Number of simulated phase shifts: $P^{(s)} = 5,\ \ s = 1, .., 10$;
- Threshold on the singular values magnitude (normalized) : $\eta = -40\,[dB]$;
- Total number of simulated AUT configurations : $K = S \times (F^{(s)} + P^{(s)}) = 10 \times (7 + 5) = 120$;

Dimension of the Over-Complete Basis

The dimension of the over-complete basis is

$$Q = 40$$

This number is given by the sum of the vectors belonging to the two considered bases:

1. Magnitude failures : $Q_1, ..., Q_{10} = 2$;
2. Phase failures : $Q_{11}, ..., Q_{20} = 2$.

Alternative (*BCS*) MbD parameters

- Toleration factor for *BCS* solver: $Tolerance = 1 \times 10^{-8}$;
- Initial noise variance for *BCS* solver: $\eta_0^{opt_1} = 10^{-2}$ and $\eta_0^{opt_2} = 5 \times 10^{-4}$. This values have been obtained as a result of a calibration procedure;

Original (*OMP*) MbD parameters

- Max. number of iterations of the OMP algorithm : $I = \{1;\ 2;\ 3;\ ...;\ 10\}$;
- Selected iteration to report the results: $I = 6$; this choice is justified by the fact that at this iteration the *OMP* algorithm reaches the best near field error as shown in the following Fig. 14.

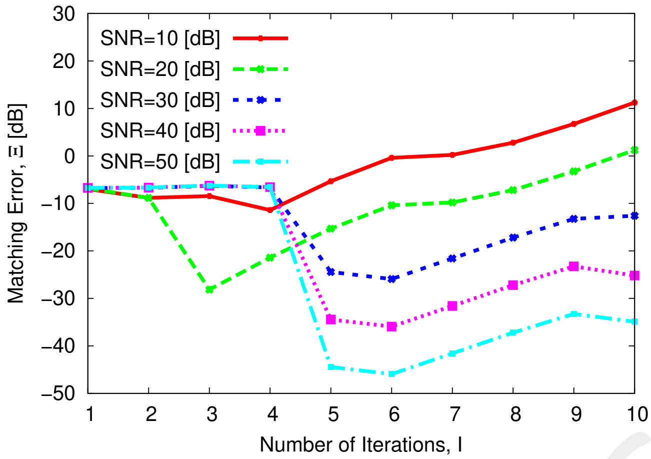

Figure 14: Behaviour of the near-field matching error versus the number of *OMP* iterations, I.

Noise

- SNR on the measured data : $SNR = \{50;\, 40;\, 30;\, 20;\, 10\}\ [dB]$;
- Noise seed : $Noise\_Seed = 63$.

2.1 Comparison between original (*OMP*) and alternative (*BCS*) MbD

Near-Field Error

The comparison, in terms of near field error, between the original (*OMP*) and the alternative (*BCS*) MbD is reported in the following Fig. 15.

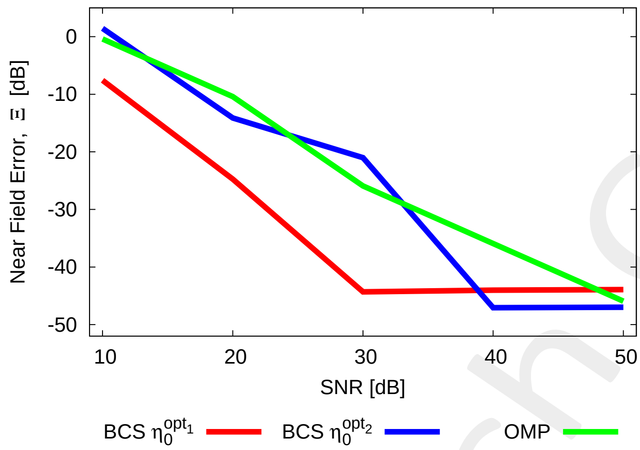

Figure 15: Near Field Error comparison between original (*OMP*) and alternative (*BCS*) MbD for different SNR values.

$SNR\,[dB]$	*Near Field Error,* Ξ $[dB]$		
	BCS		OMP
	$\eta_0^{opt_1}$	$\eta_0^{opt_2}$	
50	-43.92	-46.98	-45.93
40	-44.02	-47.07	-35.93
30	-44.32	-21.00	-25.93
20	-24.74	-14.11	-10.40
10	-7.57	1.45	-0.40

Table IV: Near Field Errors obtained by the original (*OMP*) and alternative (*BCS*) MbD

Observations

- The *OMP* algorithm is the one that in this test case achieves the worst result; in particular, the *OMP* error is quite high for $SNR < 30\,[dB]$ and good for higher *SNR* values, even its error curve is almost always above the *BCS* curves;
- About the *BCS* solver:
  - using $\eta_0^{opt_1}$, the *BCS* algorithm achieves the best result almost for the entire *SNR* range, with a remarkable ($\geq 20\,[dB]$) error difference for $SNR = 30\,[dB]$;
  - using $\eta_0^{opt_2}$, the *BCS* obtains results comparable to those of the *OMP*, except for $SNR = 40\,[dB]$ where it outperforms the *OMP*.

Estimated Near-Field

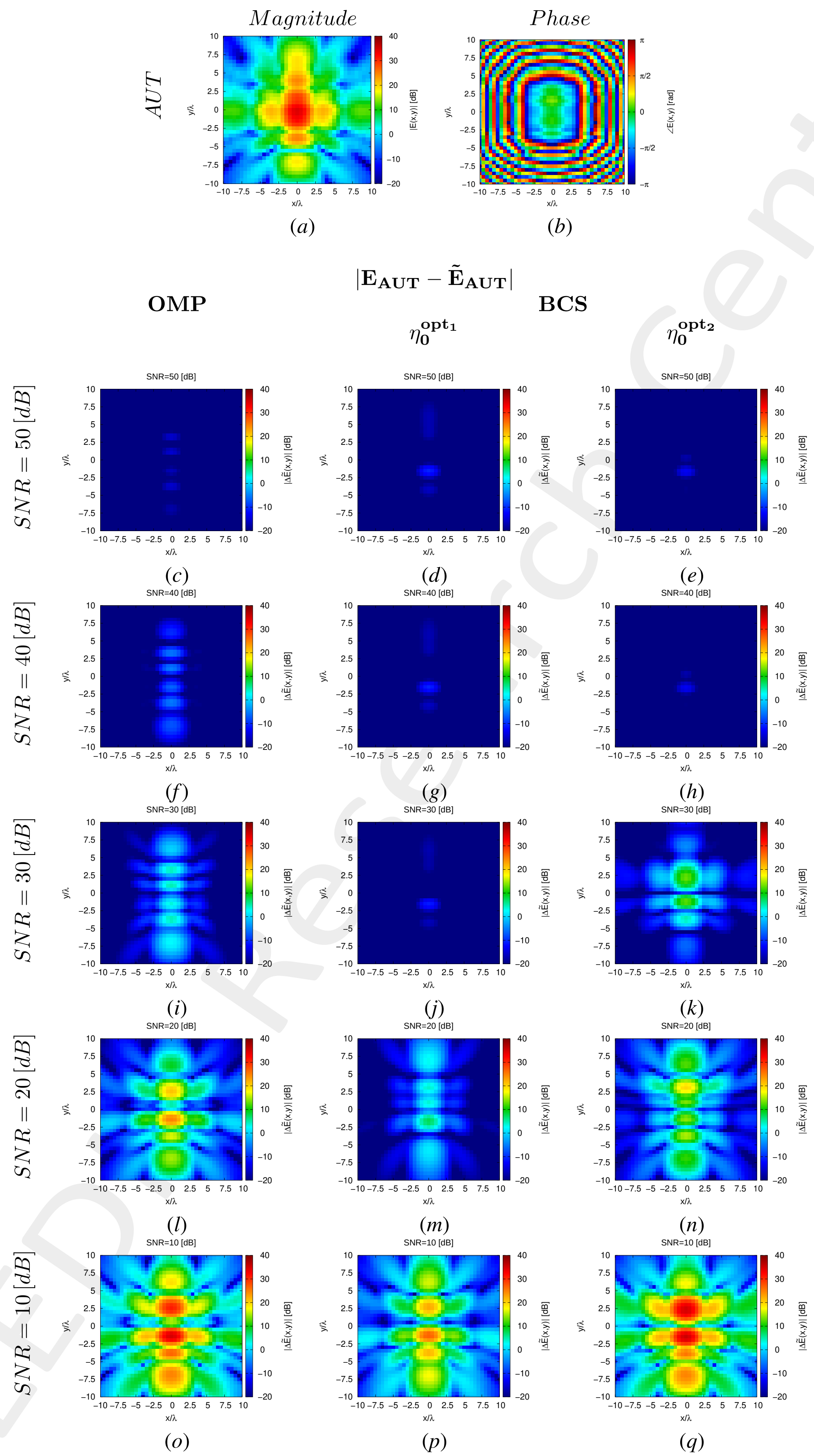

Figure 16: Magnitude difference between the actual and estimated $2-D$ near-field pattern when processing noisy measurements at different SNRs.

Estimated Coefficients

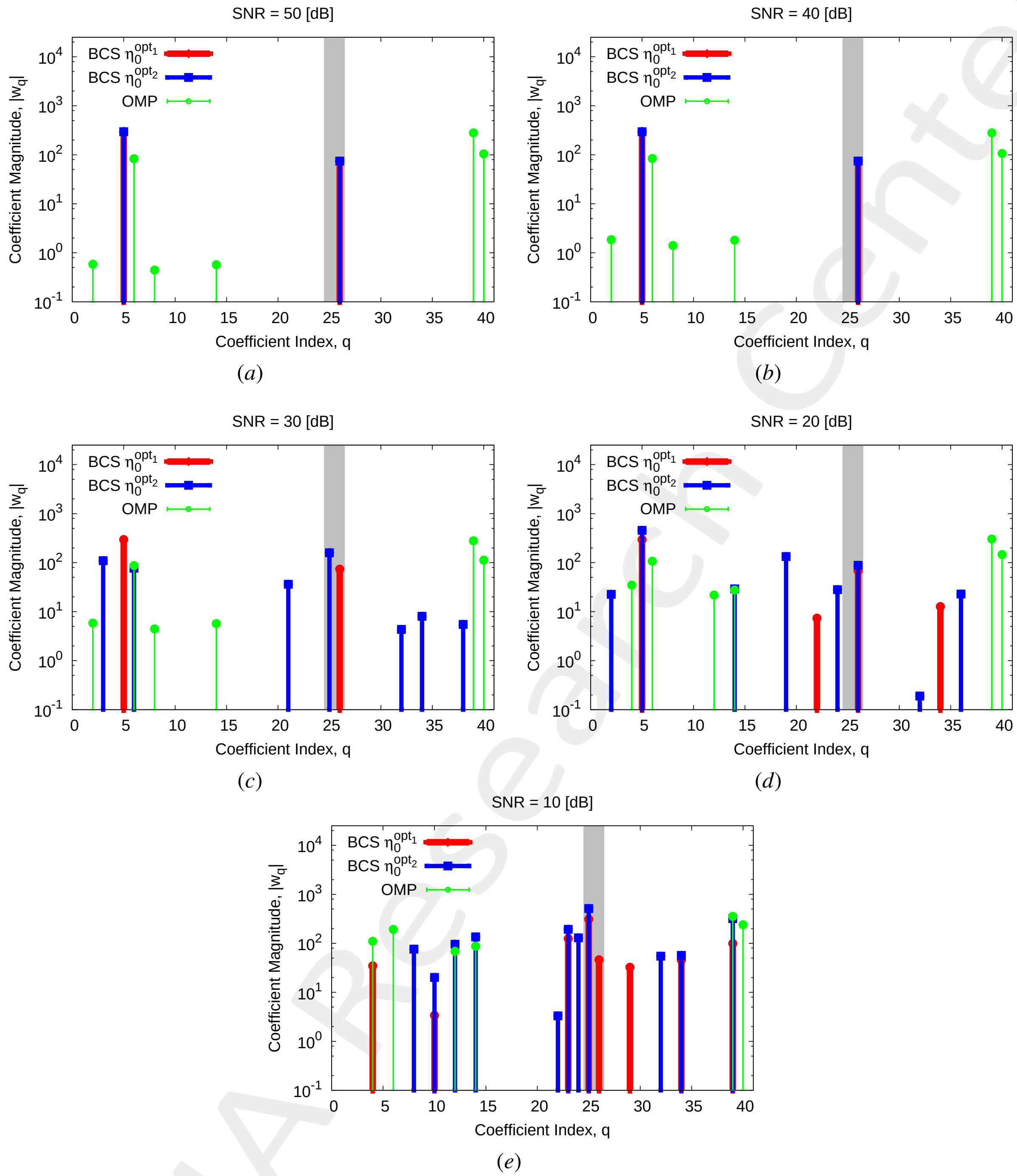

Figure 17: Coefficient comparison between original (*OMP*) and alternative (*BCS*) MbD : (*a*) $SNR = 50\,[dB]$, (*b*) $SNR = 40\,[dB]$, (*c*) $SNR = 30\,[dB]$, (*d*) $SNR = 20\,[dB]$, (*e*) $SNR = 10\,[dB]$

Observations

- The *AUT* presents only a phase failure affecting the 3^{rd} row and the *OMP* algorithm is never able to detect this failure; in particular, the *OMP* selects mainly vectors related to magnitude rather than phase failures. Moreover, the *OMP* solver always selects the same 4 vectors whatever the SNR value (vector indexes $q = 6,\ 14,\ 39,\ 40$);
- The *BCS* always detects the phase failure affecting the *AUT*, even if for low *SNR* values this detection is not precise since many other vectors are chosen by the method; independently from the value of $\eta_0$the vectors selected by the

BCS are the same for $SNR \geq 40\,[dB]$ (vector indexes $q = 5,\ 26$).

2.1.1 OMP vs best BCS

The main idea of this section is to compare the performance of the *OMP* algorithm and the best *BCS* configuration.

Near-Field Error

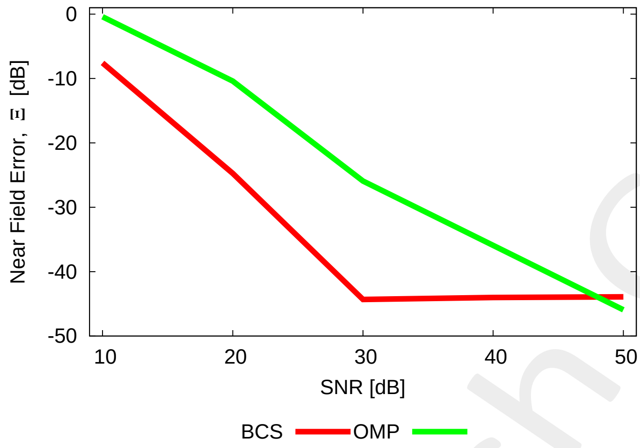

Figure 18: Near Field Error comparison between original (*OMP*) and alternative (*BCS*) MbD for different SNR values.

$SNR\,[dB]$	*Near Field Error,* Ξ $[dB]$	
	BCS	OMP
50	-43.92	-45.93
40	-44.02	-35.93
30	-44.32	-25.93
20	-24.74	-10.40
10	-7.57	-0.40

Table V: Near Field Errors obtained by the original (*OMP*) and alternative (*BCS*) MbD

Estimated Far-Field

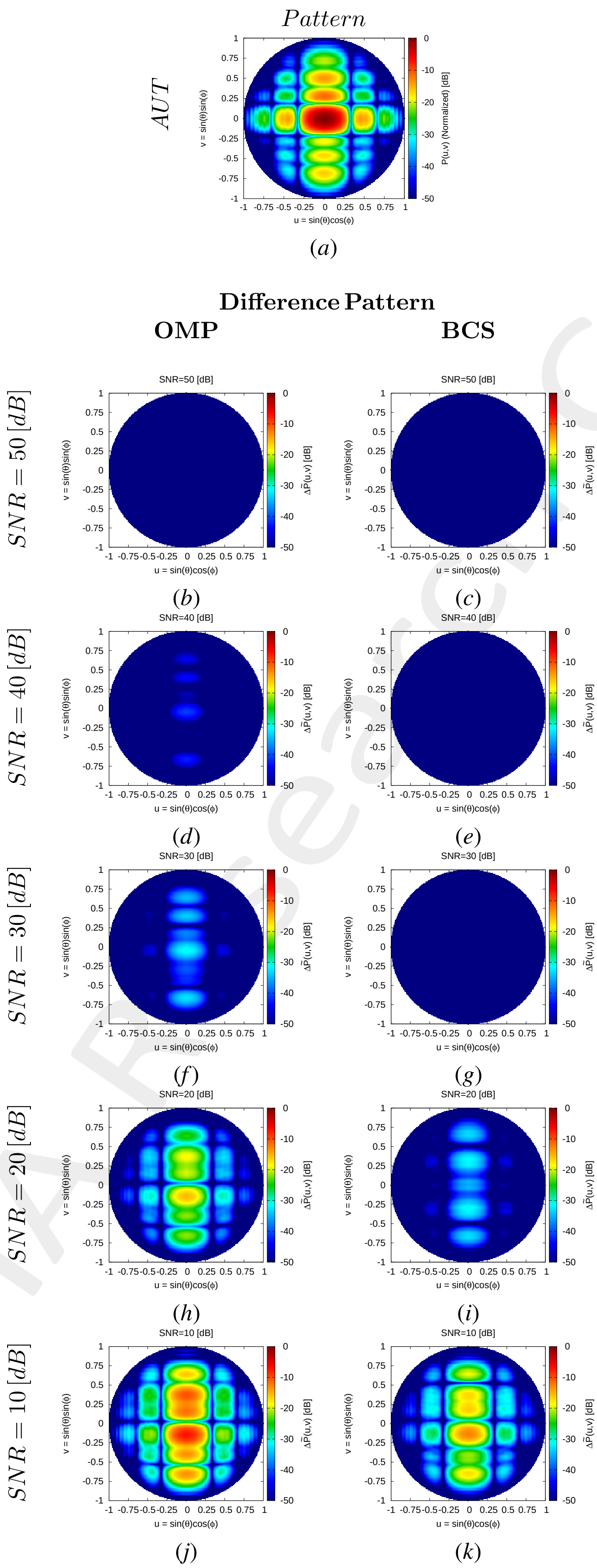

Figure 19: Difference between the actual and estimated $2-D$ far-field pattern when processing noisy measurements at different SNRs.

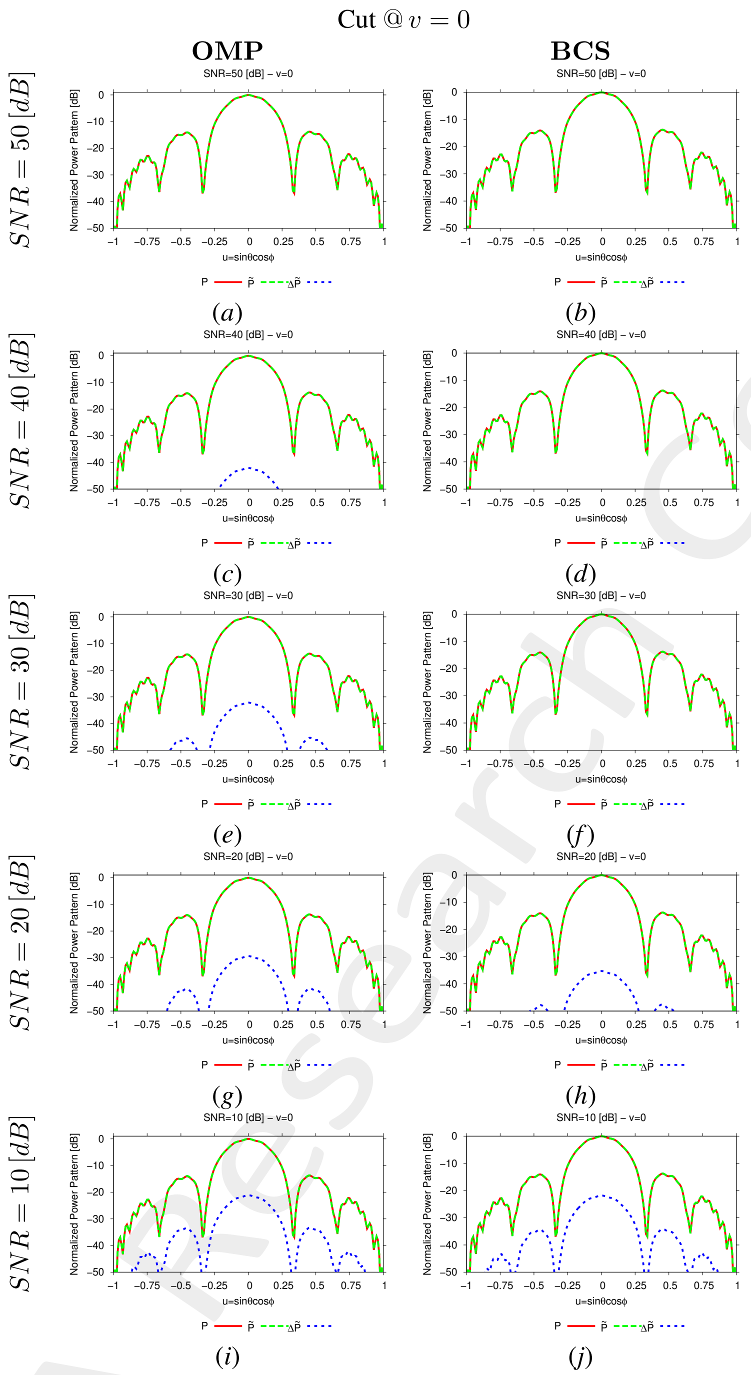

Figure 20: $1 - D$ cuts of the estimated far-field pattern (obtained through near-to-far-field transformation from the estimated near-field patterns) under several noisy conditions

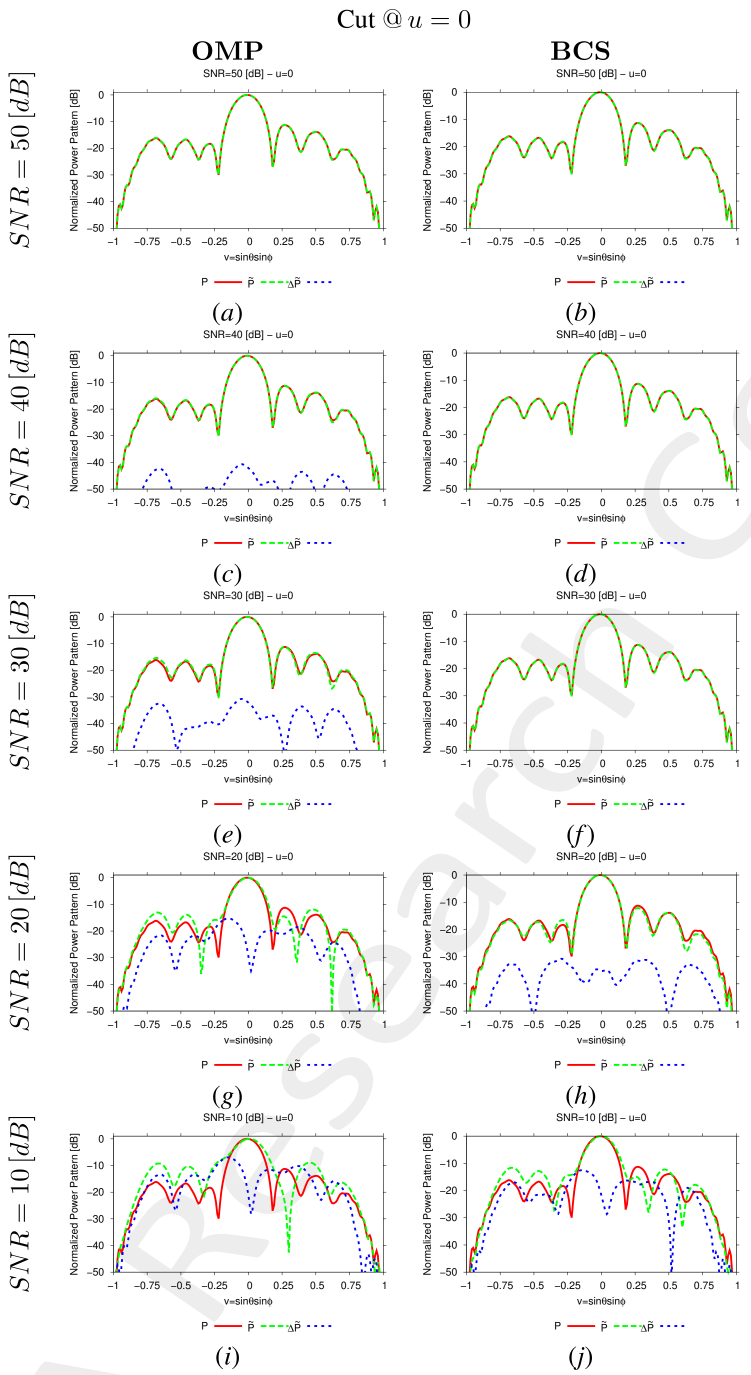

Figure 21: $1 - D$ cuts of the estimated far-field pattern (obtained through near-to-far-field transformation from the estimated near-field patterns) under several noisy conditions

$SNR\,[dB]$	$Far - Field\,Error,\,\chi\;[dB]$	
	BCS	OMP
50	-45.31	-47.28
40	-45.36	-37.30
30	-45.52	-27.37
20	-25.82	-12.35
10	-9.47	-4.06

Table VI: Far-field matching error between the actual and estimated AUT patterns (both obtained through near-to-far-field transformation from the corresponding near-field patterns) under several noisy conditions.

Estimated Coefficients

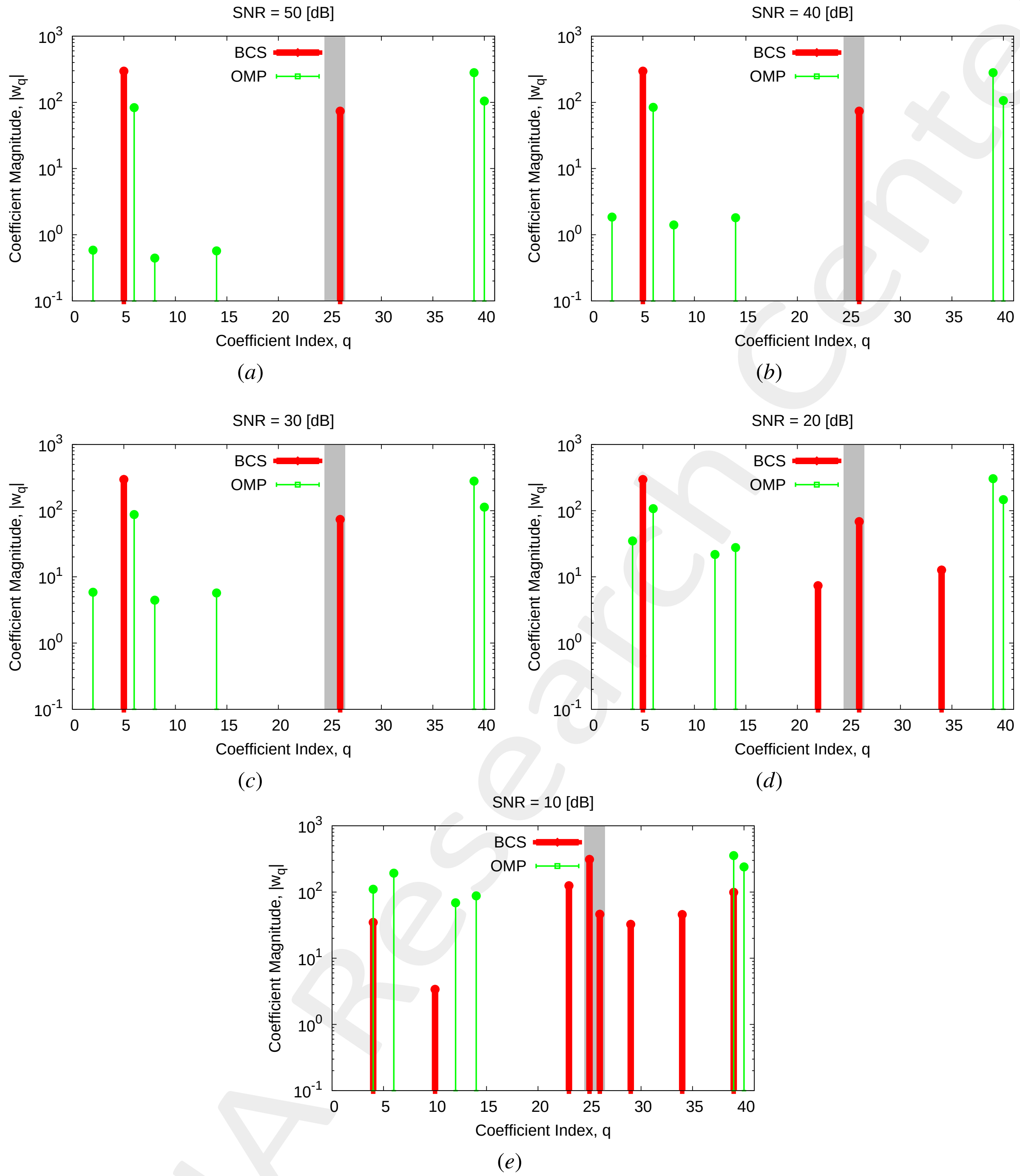

Figure 22: Coefficient comparison between original (*OMP*) and alternative (*BCS*) MbD: (*a*) $SNR = 50\,[dB]$, (*b*) $SNR = 40\,[dB]$, (*c*) $SNR = 30\,[dB]$, (*d*) $SNR = 20\,[dB]$, (*e*) $SNR = 10\,[dB]$

More information on the topics of this document can be found in the following list of references.

References

[1] M. Salucci, N. Anselmi, M. D. Migliore and A. Massa, “A bayesian compressive sensing approach to robust near-field antenna characterization,” *IEEE Trans. Antennas Propag.*, vol. 70, no. 9, pp. 8671-8676, Sep. 2022 (DOI: 10.1109/TAP.2022.3177528).

[2] B. Li, M. Salucci, W. Tang, and P. Rocca, “Reliable field strength prediction through an adaptive total-variation CS technique,” *IEEE Antennas Wirel. Propag. Lett.*, vol. 19, no. 9, pp. 1566-1570, Sep. 2020.

[3] M. Salucci, M. D. Migliore, P. Rocca, A. Polo, and A. Massa, “Reliable antenna measurements in a near-field cylindrical setup with a sparsity promoting approach,” *IEEE Trans. Antennas Propag.*, vol. 68, no. 5, pp. 4143-4148, May 2020.

[4] G. Oliveri, M. Salucci, N. Anselmi, and A. Massa, “Compressive sensing as applied to inverse problems for imaging: theory, applications, current trends, and open challenges,” *IEEE Antennas Propag. Mag. - Special Issue on "Electromagnetic Inverse Problems for Sensing and Imaging*,” vol. 59, no. 5, pp. 34-46, Oct. 2017.

[5] A. Massa, P. Rocca, and G. Oliveri, “Compressive sensing in electromagnetics - A review,” *IEEE Antennas Propag. Mag.*, pp. 224-238, vol. 57, no. 1, Feb. 2015.

[6] A. Massa and F. Texeira, “Guest-Editorial: Special Cluster on Compressive Sensing as Applied to Electromagnetics,” *IEEE Antennas Wirel. Propag. Lett.*, vol. 14, pp. 1022-1026, 2015.

[7] G. Oliveri, N. Anselmi, M. Salucci, L. Poli, and A. Massa, “Compressive sampling-based scattering data acquisition in microwave imaging,” *J. Electromagn. Waves Appl*, vol. 37, no. 5, 693-729, March 2023 (DOI: 10.1080/09205071.2023.2188263).

[8] G. Oliveri, L. Poli, N. Anselmi, M. Salucci, and A. Massa, “Compressive sensing-based Born iterative method for tomographic imaging,” *IEEE Trans. Microw. Theory Techn.*, vol. 67, no. 5, pp. 1753-1765, May 2019.

[9] M. Salucci, L. Poli, and G. Oliveri, “Full-vectorial 3D microwave imaging of sparse scatterers through a multi-task Bayesian compressive sensing approach,” *J. Imaging*, vol. 5, no. 1, pp. 1-24, Jan. 2019.

[10] M. Salucci, A. Gelmini, L. Poli, G. Oliveri, and A. Massa, “Progressive compressive sensing for exploiting frequency-diversity in GPR imaging,” *J. Electromagn. Waves Appl.*, vol. 32, no. 9, pp. 1164-1193, 2018.

[11] N. Anselmi, L. Poli, G. Oliveri, and A. Massa, “Iterative multi-resolution bayesian CS for microwave imaging,” *IEEE Trans. Antennas Propag.*, vol. 66, no. 7, pp. 3665-3677, Jul. 2018.

[12] N. Anselmi, G. Oliveri, M. A. Hannan, M. Salucci, and A. Massa, “Color compressive sensing imaging of arbitrary-shaped scatterers,” *IEEE Trans. Microw. Theory Techn.*, vol. 65, no. 6, pp. 1986-1999, Jun. 2017.

[13] N. Anselmi, G. Oliveri, M. Salucci, and A. Massa, “Wavelet-based compressive imaging of sparse targets” *IEEE Trans. Antennas Propag*., vol. 63, no. 11, pp. 4889-4900, Nov. 2015.

[14] G. Oliveri, P.-P. Ding, and L. Poli, “3D crack detection in anisotropic layered media through a sparseness-regularized solver,” *IEEE Antennas Wirel. Propag. Lett.*, vol. 14, pp. 1031-1034, 2015.

[15] L. Poli, G. Oliveri, P.-P. Ding, T. Moriyama, and A. Massa, “Multifrequency Bayesian compressive sensing methods for microwave imaging,” *J. Opt. Soc. Am. A*, vol. 31, no. 11, pp. 2415-2428, 2014.

[16] G. Oliveri, N. Anselmi, and A. Massa, “Compressive sensing imaging of non-sparse 2D scatterers by a total-variation approach within the Born approximation,” *IEEE Trans. Antennas Propag*., vol. 62, no. 10, pp. 5157-5170, Oct. 2014.

[17] L. Poli, G. Oliveri, F. Viani, and A. Massa, “MT-BCS-based microwave imaging approach through minimum-norm current expansion,” *IEEE Trans. Antennas Propag*., vol. 61, no. 9, pp. 4722-4732, Sep. 2013.

[18] F. Viani, L. Poli, G. Oliveri, F. Robol, and A. Massa, “Sparse scatterers imaging through approximated multitask compressive sensing strategies,” *Microwave Opt. Technol. Lett*., vol. 55, no. 7, pp. 1553-1558, Jul. 2013.

[19] L. Poli, G. Oliveri, P. Rocca, and A. Massa, “Bayesian compressive sensing approaches for the reconstruction of two-dimensional sparse scatterers under TE illumination,” *IEEE Trans. Geosci. Remote Sensing*, vol. 51, no. 5, pp. 2920-2936, May 2013.

[20] P. Rocca, N. Anselmi, M. A. Hannan, and A. Massa, “Conical frustum multi-beam phased arrays for air traffic control radars,” *Sensors*, vol. 22, no. 19, 7309, pp. 1-18, 2022 (DOI: 10.3390/s22197309)

[21] F. Zardi, G. Oliveri, M. Salucci, and A. Massa, “Minimum-complexity failure correction in linear arrays via compressive processing,” *IEEE Trans. Antennas Propag*., vol. 69, no. 8, pp. 4504-4516, Aug. 2021.

[22] N. Anselmi, G. Gottardi, G. Oliveri, and A. Massa, “A total-variation sparseness-promoting method for the synthesis of contiguously clustered linear architectures,” *IEEE Trans. Antennas Propag*., vol. 67, no. 7, pp. 4589-4601, Jul. 2019.

[23] M. Salucci, A. Gelmini, G. Oliveri, and A. Massa, “Planar arrays diagnosis by means of an advanced Bayesian compressive processing,” *IEEE Trans. Antennas Propag*., vol. 66, no. 11, pp. 5892-5906, Nov. 2018.

[24] L. Poli, G. Oliveri, P. Rocca, M. Salucci, and A. Massa, “Long-Distance WPT Unconventional Arrays Synthesis,” *J. Electromagn. Waves Appl*., vol. 31, no. 14, pp. 1399-1420, Jul. 2017.

[25] G. Oliveri, M. Salucci, and A. Massa, “Synthesis of modular contiguously clustered linear arrays through a sparseness-regularized solver,” *IEEE Trans. Antennas Propag.*, vol. 64, no. 10, pp. 4277-4287, Oct. 2016.

[26] M. Carlin, G. Oliveri, and A. Massa, “Hybrid BCS-deterministic approach for sparse concentric ring isophoric arrays,” *IEEE Trans. Antennas Propag.*, vol. 63, no. 1, pp. 378-383, Jan. 2015.

[27] G. Oliveri, E. T. Bekele, F. Robol, and A. Massa, “Sparsening conformal arrays through a versatile BCS-based method,” *IEEE Trans. Antennas Propag.*, vol. 62, no. 4, pp. 1681-1689, Apr. 2014.

[28] F. Viani, G. Oliveri, and A. Massa, “Compressive sensing pattern matching techniques for synthesizing planar sparse arrays,” *IEEE Trans. Antennas Propag.*, vol. 61, no. 9, pp. 4577-4587, Sept. 2013.

[29] P. Rocca, M. A. Hannan, M. Salucci, and A. Massa, “Single-snapshot DoA estimation in array antennas with mutual coupling through a multi-scaling BCS strategy,” *IEEE Trans. Antennas Propag.*, vol. 65, no. 6, pp. 3203-3213, Jun. 2017.

[30] M. Carlin, P. Rocca, G. Oliveri, F. Viani, and A. Massa, “Directions-of-arrival estimation through Bayesian Compressive Sensing strategies,” *IEEE Trans. Antennas Propag.*, vol. 61, no. 7, pp. 3828-3838, Jul. 2013.

[31] M. Carlin, P. Rocca, G. Oliveri, and A. Massa, “Bayesian compressive sensing as applied to directions-of-arrival estimation in planar arrays," *J. Electromagn. Waves Appl.*, vol.2013, pp.1-12, 2013 (DOI :10.1155/2013/245867).